3D reconstruction of a gas diffusion layer and a microporous layer

H. Ostadi, K. Jiang

School of Mechanical engineering, University of Birmingham, Birmingham, B15 2TT, UK

P. Rama, Y. Liu, R. Chen

Department of Aeronautical and Automotive Engineering, Loughborough University, Leicestershire, LE11 3TU, UK

X. X. Zhang

Department of Engineering, University of Liverpool, Brownlow Street, L69 3GH, UK.

Abstract:

The focus of the current study is on a state-of-the-art twin-layer gas diffusion layer (GDL) which consists of carbon tissues with a fibre diameter of 5~20 μm, and contains a microporous layer (MPL) coating which has sub-micron porous features. In the current study, real-world digital three-dimensional images of the GDL-MPL assembly are created through X-ray nano-tomography with a 680 nm pixel resolution for the GDL and focused ion beam/scanning electron microscopy (FIB/SEM) nano-tomography with a 14 nm pixel resolution for the MPL. The critical nano-structural features including porosity, characteristics lengths and 3D pore size distribution are determined directly from the 3D digital representation. In addition to morphological parameters, the FIB/SEM nanotomography technique has been combined with lattice Boltzmann (LB) numerical modelling in order to calculate the tortuosity and permeability of the MPL.

Keywords: Gas diffusion layer, Microporous layer, FIB/SEM nano-tomography, X-ray nano-tomography, Lattice Boltzmann numerical modeling.

1. Introduction

The polymer electrolyte fuel cell (PEFC) is composed of four primary types of components; the polymer electrolyte membrane (PEM), the catalyst layer (CL), the GDL and the MPL. The PEM is a proton-conductor which separates the anode and cathode electrodes of the PEFC. The anode and cathode CLs are carbon agglomerate-based layers which hosts the hydrogen-oxidation and oxygen-reduction reactions respectively. The MPL is a carbon-based nano-porous medium with a high degree of hydrophobicity which plays a key role in transporting reactant gases and excess water to and from the adjacent CL as well as providing pathways for electron conduction. The GDL is similar in nature to the MPL and serves a similar role but is much less hydrophobic and has a greater porosity than the MPL [1,2].

Although numerous models have been developed to describe the behaviour of GDL-MPL layers in terms of fluid transportation and fuel cell performance at micro/nano-scale [2-7], the models are all commonly dependant on the use of key parameters such as porosity, mean pore radius, tortuosity, permeability and effective diffusivity which are all determined by the micro/nano-structural characteristics of the material [8-12]. Such parameters cannot be rigorously determined without the real 3D structure. For example, it is nearly impossible to determine the tortuosity of porous pathways using 2D images alone because it is controlled by how the porous network is interconnected in 3D. Determining the pore size distribution and mean pore radius of both the GDL and MPL also commands a full understanding of the 3D structure. In porous electrode theory, such parameters are usually estimated based on idealized models or assumed to be adjustable parameters. Other methods based on stochastic three-dimensional reconstruction [13] do not closely reflect nano-structural properties and it is difficult to apply such technique to understand how improved structures could give improved performance.

Recently, X-ray micro-tomography [14] has been used to quantify liquid water saturation in GDLs and in determining two-phase material parameters with ~10 μm resolution. However, the results suggest that the technique requires much more development and better resolution for application to fuel cells [15]. X-ray nanotomography with a spatial resolution of 700 nm has been successfully employed to determine the permeability and diffusivity of the GDL layer as a function of the saturation of the layer [16]. However in that study, the MPL was not considered.

The sub-micron features of the MPL require visualisation with a sub-25 nm resolution. The most recent X-ray synchrotron facilities cannot provide a resolution better than ~50 nm [17]. In addition, the soft nature of the layer makes it difficult to prepare thin samples suitable for X-ray nano-tomography. In order to visualise the nano-structural features of the porous network of an MPL without extensive sample preparation, a dual-beam FIB/SEM nano-tomography was employed in this work [18,19]. The method has been used for the characterisation of solid oxide fuel cell (SOFC) anodes and the calculation of critical micro-structural features [20].

2. Experimental

A 300 µm thick developmental GDL supplied by Technical Fibre Products (TFP, Technical Fibre Products Ltd., UK) with a developmental MPL applied by Johnson Matthey Fuel Cells (JMFC, Johnson Matthey Fuel Cells Ltd., UK) was used in this study. A 1 mm^2 sample was imaged using a SkyScan 2011 desktop nano-tomography system (SkyScan, Belgium), with a source voltage of 25 kV, a current of 200 µA and no filtering of the X-rays. On average 3 frames of 2 sec exposure time were acquired at each 0.5° rotation step. This generated 371 shadow images with a pixel size resolution of 680 nm in around 45 minutes. The tomography images were then processed using CTAN software (Skyscan, Belgium) to reconstruct a 3D digital model of the sample, as shown in Figure 1.

For the 10 µm thick MPL, a dual-beam FIB/SEM system (FEI Dual Beam Strata 235, FEI Company, US) has been used as a nano-tomography tool to obtain the 3D structure of a ~10 µm3 sample. The process involved milling away a thin slice (~14 nm) of the side-wall of a trench using FIB and recording an SEM image of the new surface, then repeatedly milling and imaging to produce a stack of SEM images. The surface was coated by 100 nm-thick layer of platinum prior to side-wall milling in order to protect the soft surface from ion bombardment and to reduce the re-deposition effect caused by FIB-induced decomposition of the precursor gases. The Pt layer also serves to suppress curtaining effects [21]. Each slice of the sample is milled-off with FIB Ga+ ion beam at 30 kV and 50 pA for 45 sec and a dwell time of 1 µsec. 100 slices with a total thickness of ~1.5 µm were removed and SEM images of the slices with ~8 nm each pixel size were taken. The edge of the milled side wall was used as a fiducial mark to align the images. The 2D aligned images were then thresholded and used to build a 3D binary image with 0 and 1 representing pore and solid phases respectively. The 3D reconstructions of the layer were carried out and the key nano-structural properties determined.

3. Imaging Results

Figure 2 shows the FIB/SEM and the sample configuration. In figure 3a, the pores on the side wall, the deposited platinum on the MPL surface and the fiducial mark are shown. A 3D reconstruction of the MPL with pores (light grey) and solid phase (dark grey) are presented in figures 3b. The white lines show the connectivity and tortuous pore network in the porous media.

4. Key nano-structural features

With an accurate digital representation of the 3D structure at hand, it is subsequently possible to determine the critical features of the assembly. The porosity of the GDL plays a key role in fuel cell performance. The porosity obtained from X-ray nano-tomography using CTAN software varies between 81~85% depends on threshold alterations. The threshold indicates a level on the greyscale which separates void space from solid space and is applied to the collection of X-ray images in order to generate the binary 3D model from the greyscale images. The choice of threshold level is usually determined heuristically involving visual inspection [15,16]. In our investigation, the threshold was fine-tuned to match the porosity of the resulting binary 3D model to the measured porosity based on a density calculation of 84%. Hence the threshold was fixed at a value where the porosity of the 3D structure is achieved as 84%. The corresponding local porosity value for the MPL attained from FIB/SEM nano-tomographic 3D reconstruction was ~40%.

The local effective diffusivity of a gas (D_{eff,H_2}, D_{eff,O_2}, D_{eff,H_2O}) is a function of the porosity and level of liquid water saturation in GDL. Its value can be estimated using the Tomadakis and Sotirchos (TS) approach [7,23]:

$$D_{eff} = D_{gas}\varepsilon((\varepsilon - 0.11)/0.89)^{0.785}(1 - s)^2 \quad (1)$$

where the multiple of gas D_{gas} on the right hand side can be referred to as the TS effective diffusivity factor, k_{TS}.

Figure 4 shows the dependence of k_{TS} on liquid saturation using the porosities of the GDL and MPL of 84% and 40% as deduced from the reconstructed digital images. The gas diffusivities [9] of hydrogen, oxygen and water vapour can be determined as 114.0 mm^2/s, 34.5 mm^2/s and 30.3 mm^2/s

respectively. With 50% saturation, therefore, the effective diffusivity of the gases reduces to 20.0 mm^2/s, 6.21 mm^2/s and 5.45 mm^2/s in the GDL and 4.6 mm^2/s, 1.4 mm^2/s and 1.2 mm^2/s in the MPL.

In order to determine the absolute through-plane permeability [1] of a GDL without the MPL, controlled pressure-drop measurements were carried out for a 10×10 cm^2 sample using a Frazier air tester. The calculated permeability of the GDL based upon direct measurement was obtained as 1.86×10-5 mm^2. The permeability can also be calculated using structural parameters obtained from the binary 3D model of a layer through the empirical Kozeny-Carman relation [24]:

$$K = \varepsilon^2 d_f^2 / 16 k_K (1-\varepsilon)^2 \quad (2)$$

where d_f, ε and k_K are average fibre/agglomerate diameter, porosity and Kozeny constant. The average fibre diameter based on X-ray nano-tomography is obtained as 7.3 μm. The literature demonstrates a wide scatter in the value of Kozeny constant for GDL materials in general ranging from 1.45 to 26.50, but in the region of 4.06 to 4.54 for typical commercial materials based on carbon fibres [25]. Taking the median value of the reported values of 4.26 the through-plane permeability based on the Kozeny-Carman relation is 1.83×10-5 mm^2. The exact figure of 1.86×10-5 mm^2 is achieved when the Kozeny constant is set to 4.16. For the MPL, the determination of permeability through controlled pressure measurement drop is formidable because of the thinness of the layer (10 μm). However, the FIB/SEM nano-tomography reveals an average diameter of ~165 nm for the MPL and assuming that the Kozeny constant is 5, the corresponding value of permeability can be calculated as 5.20×10-11 mm^2.

The characteristic capillary radius [9] is expressed by:

$$r_c = 2\sqrt{K/\varepsilon} \quad (3)$$

where K is the absolute permeability. The calculated permeability along with the porosity data from X-ray and FIB/SEM nano-tomography results in capillary radii of ~7.5 μm and ~22 nm for the GDL and MPL respectively. This means that the capillary pressure ($P_c \propto 1/r_c$) in the MPL is ~300 times larger than GDL layer and may prevent any liquid from entering the MPL.

Pore size distribution is a key characteristic of GDL and MPL assemblies [2,6,26]. The pore size distribution has been found based on X-ray nano-tomography results through CTAN software for the GDL layer as shown in figure 5a. 12% of the pores are less than 7 μm (micropores and mesopores), 83% are between 7 μm and 20 μm (macropores) and finally 5% are more than 20 μm. An average size of ~15 μm was obtained for GDL mean pore diameter. Although mass-transport limitations can be reduced by enlarging the macropores [6, 27], the large pores can also result in a decrease of the electrical conductivity of the electrode. The literature [28] also suggests that serious water flooding can occur in GDL when the mean pore diameter is greater than 30 μm.

For the MPL, the pore size distribution is as follows: 23% of the pores are less than 120 nm in diameter, 52% are between 120 to 220 nm and 25% are more than 220 nm in diameter as shown in figure 5b. The average size of the pore diameter was found as 137 nm. It has been recently found [29] that porosity-graded MPL can result in improved electrode process of fuel cell reaction in comparison with those with conventional homogeneous MPL, particularly at high current densities. This may caused by facilitating the transportation of water in the large pores and diffusion of gas through small pores.

According to the kinetic theory of gases [3], the Knudsen diffusion coefficient in MPL, is a linear function of the mean pore radius:

$$D_K = \frac{2}{3} r \sqrt{8RT/\pi M} \quad (4)$$

Where r, R, T and M are mean pore radius, gas constant, temperature in Kelvin and molar mass of air. Hence, the Knudson diffusion coefficient of the MPL is calculated as 0.5 cm^2/s.

5. Calculation of fluid transport parameters

The final part of this study focuses on the application of a numerical technique to further-examine the structural properties of the layer and single-phase fluidic properties. This was conducted through the application of the lattice Boltzmann [30,31] numerical solver to simulate single-phase flow through the porous network of the layer and calculate the permeability and tortuosity [10] of the MPL.

The LB method is a numerical algorithm that has been developed over the past two decades to simulate fluid dynamics based on kinetic theory [32]. The concept of the LB method was introduced by McNamara and Zanetti [33] in order to overcome some drawbacks of its predecessor, the lattice gas algorithm [34]. It was found later that the LB method can be derived directly from the continuous Boltzmann equation in kinetic theory. Unlike conventional computational fluid dynamics, the LB method does not directly solve the partial differential equations. Instead, it simulates fluid dynamics by tracking the movement and collisions of a number of fictitious particles in a lattice. The spatiotemporal distributions of entities such as fluid density and velocity are calculated through the sum of the corresponding moments of all the particles at each node. With the LB method it is relatively facile to deal with complicated boundaries and various forces acting at microscopic scales and overall therefore it becomes more efficient to simulate complex flows in porous media at pore scale.

In this study, the lattice is taken directly as the binary 3D image of the MPL sample of 2.7 μm^3 and the simulation is carried out in the D3Q19 scheme which simulates 3D flow by considering nineteen velocities originating from each point in the lattice. In a previous study [35], the LB technique was applied to determine the permeability of the GDL X-ray micro-tomography images and was subsequently validated against the permeability calculated using controlled pressure drop measurements. The validated technique is applied here to characterise the MPL. The simulated permeability in the through-plane direction is determined as 5.44×10-10 mm^2. The simulated permeability in the off-principal in plane directions is calculated as 8.99×10-12 mm^2 and 2.70×10-11 mm^2 resulting in an RMS off-principal value of 2.01×10-11 mm^2. The calculated through-plane permeability is one order of magnitude greater than that suggested by the Carman-Kozeny equation when the Kozeny constant is assumed to hold a value of 5. The literature does not explicate an understanding of what value the Kozeny constant should hold for MPL materials. However, the literature suggests that the Kozeny constant can depart from the commonly assigned value of 5 and decrease to less than unity as the interconnectivity and porous structure of the material becomes increasingly complex [36], which is clearly the case for the MPL when compared to the GDL. As such, the current study suggests that the exact figure of 5.44×10-10 mm^2 as obtained from the through-plane LB simulation can be achieved from the Kozeny-Carman equation when the Kozeny constant is set equal to 0.48. On a similar note, the LB calculations suggest that the permeability in the through-plane direction is one order of magnitude greater than the RMS value of the in-plane directions. The

results therefore suggest that the MPL is preferentially structured to allow flow to propagate in the through-plane direction. The LB results also show that the through-plane permeability is 5 orders of magnitude lower in the MPL than in the GDL.

The LB technique applied to determine the tortuosity of the MPL is fundamentally the same as that applied to calculate permeability described elsewhere [34,35] but simplified to consider seven velocities in three dimensions (D3Q7). In addition, the equilibrium distribution function, $f_i^{eq}(x,t)$, for fictitious particles moving with through the lattice can be defined as:

$$f_i^{eq}(x,t) = c/7 \tag{6}$$

where 7 represents the number of directions (including the stagnant particles) along which the particles move and c is the gas concentration, calculated by:

$$c = \sum_{i=0}^{6} f_i(x,t) \tag{7}$$

where $i = 0$ represents the stagnant particles and $i = 1-6$ represent the mobile particles. The free diffusion coefficient of gas movement in the void space is given by:

$$D_0 = 2\delta x^2(\tau - 0.5)/7\delta t \tag{8}$$

Where δt and δx are time step and the characteristic length of a cubic voxel respectively. τ is a dimensionless parameter that controls the rate of $f_i(x,t)$ approaching $f_i^{eq}(x,t)$. The diffusive gas flux , J , in each void voxel is calculated by:

$$J = (1 - 1/2\tau)\sum_{i=1}^{6} \xi_i f_i \tag{9}$$

Two different gas concentrations can be applied to the two opposing faces of the structure, which in return drives a diffusive flow through the simulated structure. The remaining four faces of the 3D image can be treated as periodic boundaries, in an identical manner to that described for the permeability analysis [35]. The voidsolid interface is assumed to be impermeable to the gas. After the gas flow is deemed to have reached steady state, the effective diffusion coefficients of the gas in direction i along which the gas concentration gradient was applied can be estimated as:

$$D_{ii} = \frac{L}{N\Delta c}\sum_{n=1}^{N} J_{i,n} \quad (10)$$

where N is the total number of the void voxels in the image, Δc is the concentration difference applied to the two opposite faces, L is the distance between the two faces, and $J_{i,n}$, is the flux in the i direction at voxel n when the concentration gradient is applied in the i direction. With the effective diffusion coefficient of gas flow in the structure and the free diffusion coefficient known, the tortuosity of the porous network along the direction i is calculated by

$$\lambda_i = D_0/D_{ii} \quad (11)$$

Hence, by combining the full 3D morphological reconstruction of the structure with LB-based numerical flow simulation, the resulting calculation of tortuosity based on diffusion will directly reveal the convolution of pathways within the porous structure in all three dimensions.

The LB simulation suggests that the tortuosity of the MPL in the principal flow direction is 1.36, and 1.53 and 1.60 in the two off-principal directions. The results suggest that the toruosity is 13% less in the principal through-plane direction in comparison to the RMS tortuosity in the off-principal directions.

Figure 6 illustrates the flow paths in the principal through plane and the two off-principal directions through the MPL. The difference in tortuosity can be confirmed by closely examining the linearity of the flow paths in figure 6a compared to figures 6b and 6c.

6. Conclusions

The current study demonstrates that the actual 3D structure of the fuel cell GDL and MPL can be captured through X-ray and FIB/SEM nano-tomography respectively. A binary 3D model of the complex structures can be generated using software techniques and by threshold-tuning the greyscale X-ray images by matching the porosity of the resultant 3D model with the measured porosity of the real sample. It has been successfully demonstrated that key structural data can be generated using the 3D model such as average fibre diameter and pore size distribution. The effective diffusivity, absolute permeability and characteristic capillary radii have also been obtained from directly-measured data from the 3D model. The theoretical permeability of the GDL agrees well with measurement and suggests a Kozeny constant of 4.16. The LB numerical solver is subsequently

applied to simulate the permeability of the MPL. The simulated permeability of the MPL suggests that the Kozeny constant for this layer is one order of magnitude less than that expected for the GDL. The LB numerical solver is also applied to visualise the tortuosity of the flow paths through the MPL. The current study elucidates the potential to enable improvements in GDL-MPL assembly design, material composition and cell design to be realised through a greater understanding of the nano-scale transport processes occurring within the PEFC.

7. Acknowledgments

This research was supported by the UK Technology Strategy Board (TSB Project No.: TP/6/S/K3032H). We acknowledge industrial partners AVL List GmbH, Intelligent Energy Ltd., Johnson Matthey Fuel Cells Ltd., Saati Group Inc. and Technical Fibre Products Ltd. for their support of this work.

References

[1] M. F. Mathias, J. Roth, J. Fleming, W. Lehnert, Handbook of Fuel Cells-Fundamentals, Technology and Application Vol.3 (Eds W. Vielstich, A. Lamm and H. A. Gasteiger) John Wiley and Sons, Chichester, England (2003) 517.

[2] A. Z. Weber, J. Newman, J. Electrochem. Soc. 152 (2005) 677.

[3] A. Z. Weber, J. Newman, Chem. Rev. 104 (2004) 4679.

[4] Z. Zhan, J. Xiao, Y. Zhang, M. Pan, R. Yuan, Int. J. Hydrogen. Energ. 32 (2007) 4443.

[5] U. Pasaogullari, P. P. Mukherjee, C. Y. Wang, K. S. Chenc, J. Electrochem. Soc. 154 (2007) 823.

[6] C. S. Kong, D. Y. Kim, H. K. Lee, Y. G. Shul, T. H. Lee, J. Power Sources. 108 (2002) 185.

[7] J. H. Nam, M. Kaviany, Int. J. Heat. Mass. Tran. 46 (2003) 4595.

[8] J. M. Zalc, S. C. Reyes, E. Iglesia, Chem. Eng. Sci. 59 (2004) 2947.

[9] C. Y. Wang, Chem. Rev. 104 (2004) 4727.

[10] J. B. Young Annu. Rev. Mater. Res 39 (2007) 19.

[11] P. K. Sinha, P. P. Mukherjee, C. Y. Wang, J. Mater. Chem. 17 (2007) 3089.

[12] D. M. Bernardi, M. W. Verbrugge, AIChE J. 37 (1991) 1151.

[13] R. Thiedmann, F. Fleischer, C. Hartnig, W. Lehnert, V. Schmidt, J. Electrochem. Soc. 155 (2008) 391.

[14] W. S. Haddad, I. McNulty, J. E. Trebes, E. H. Anderson, R. A. Levesque, L. Yang ,Science. 266 (1994) 1213.

[15] P. K. Sinha, P. Halleck, C. Y. Wang, Electrochem. Solid. St. 9 (2006) A344.

[16] J. Becker, V. Schulz, A. Wiegmann, J. Fuel Cell Sci. Tech. 5 (2008) 1.

[17] E. Zschech, W. Yun, G. Schneider, Appl. Phys. A-Mater. 92 (2008) 423.

[18] E. L. Principe Focused ion beam systems basics and applications, (Ed N. Yao) Cambridge Press, Cambridge, England, (2007) 146.

[19] A. J. Kubis, G. J. Shiflet, D. N. Dunn, R. Hull, Metall. Mater. Trans. A. 35A (2004) 1935.

[20] J. R. Wilson, W. Kobsiriphat, R. Mendoza, H. Y. Chen, J. M. Hiller, D. J. Miller, K. Thornton, P. W. Voorhees, S. B. Adler, Nat. Mater. 5 (2006) 541.

[21] R. Langford, Focused ion beam systems basics and applications, (Ed N. Yao) Cambridge Press, Cambridge, England (2007) 215.

[22] H. Ostadi, K. Jiang, P. D. Prewett, Micro Nano Lett. 3 (2008) 106.

[23] M. M. Tomadakis, S. V. Sotirchos, AIChE J. 39 (1993) 397.

[24] M. Kaviany, Principles of heat transfer in porous media, second ed., Springer, New York, USA (1999) 101.

[25] J. T. Gostick J T, M. W. Fowler, M. D. Pritzker, M. A. Ioannidis, L. M. Behra, J. Power Sources 162 (2006) 228.

[26] A. Z. Weber, R. M. Darling, J. Newman, J. Electrochem. Soc. 151 (2004) 1715.

[27] D. M. Bernardi, M. W. Verbrugge, J. Electrochem. Soc. 139 (1992) 2477.

[28] M. S. Wilson, J. A. Valerio, S. Gottesfeld, Electrochim. Acta 40 (1995) 355.

[29] H. Tang, S. Wang, M. Pan, R. Yuan, J. Power Sources 166 (2007) 41.

[30] X. Nie, G. Doolen, S. Chen, J. Stat. Phys. 107 (2002) 279.

[31] P. P. Mukherjee, C. Y. Wang, Q. Kang, Electrochim. Acta 54 (2009) 6861.

[32] H. Chen , S. Chen, W. H. Matthaeus, Phys. Rev. A. 45 (1992) 533.

[33] G. R. McNamara, G. Zanetti, Phys. Rev. Lett. 61 (1998) 2332.

[34] U. Frisch, B. Hasslacher, Y. Pomeau, Rev. Lett. 56 (1986) 1505.

[35] P. Rama, Y. Liu, R. Chen, H. Ostadi, K. Jiang, X. Zhang, R. Fisher, M. Jeschke, J. Fuel. Cell. Sci. Tech. 7 (2010) In press.

[36] A. W. J. Heijs, C. P. Lowe, Phys. Rev. E. 51(5) (1995) 4346.

Figure 1. 3D reconstruction of a GDL carbon paper of 300 μm×700 μm×900 μm (X,Y,Z) using desktop X-ray Nanotomography with 680 nm resolution.

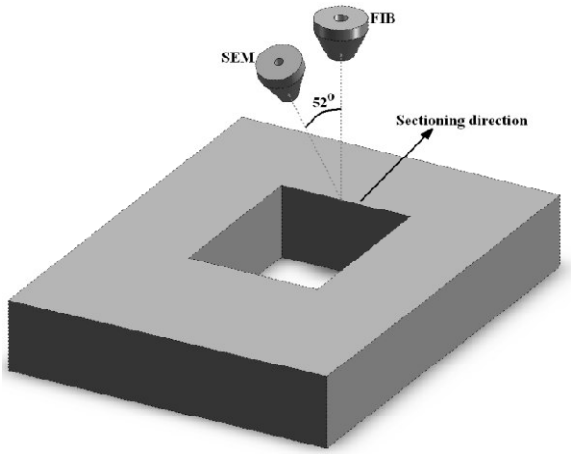

Figure 2. FIB/SEM and sample configuration. After milling a 25 μm×25 μm cube and deposit a 100 nm protective layer of Pt, 100 SEM images of the MPL side walls were acquired repetitively after milling thin slices of ~14 nm thickness each. The sectioning direction was perpendicular to FIB column.

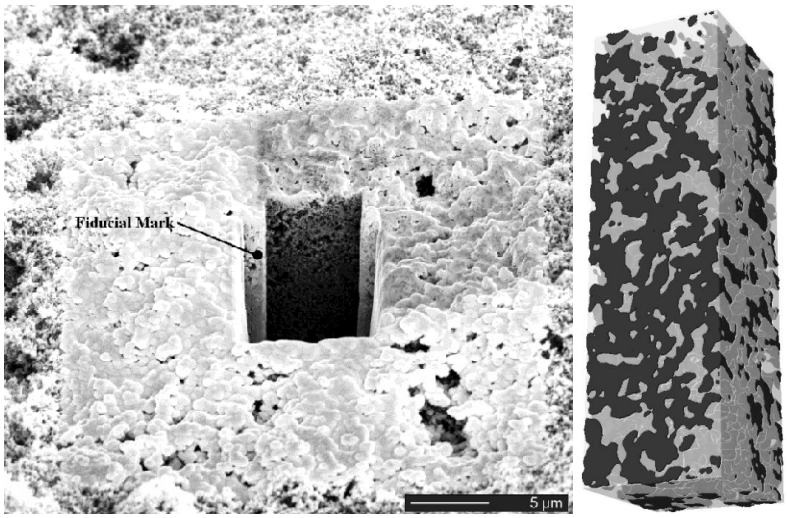

a b

Figure 3. a) Low magnification SEM image of the trench side wall polished through low current 50 pA ion beam. A 25 µm×25 µm area with 100 nm thick of Platinum was deposited on the surface. The fiducial mark is used for image alignment; b) a 1.5 µm×1.5 µm× 5 µm 3D reconstructed image of the MPL with 14 nm× 8 nm×8 nm voxel size. Dark and light grey show solid and pore networks respectively. The tortuous white lines shows how the pore network is interconnected.

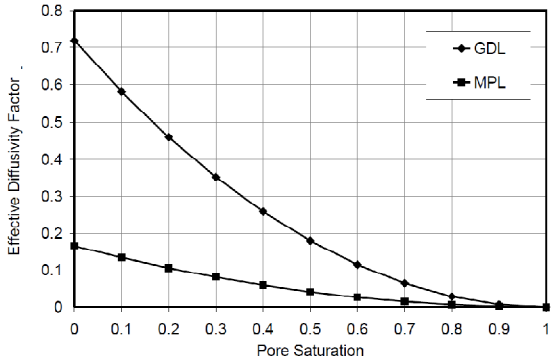

Figure 4. Calculated Tomodakis Sotirchos effective diffusivity factor as a function of liquid saturation for the reconstructed models of the GDL and MPL using Equation (1). GDL and MPL porosities are 84% and 40% respectively.

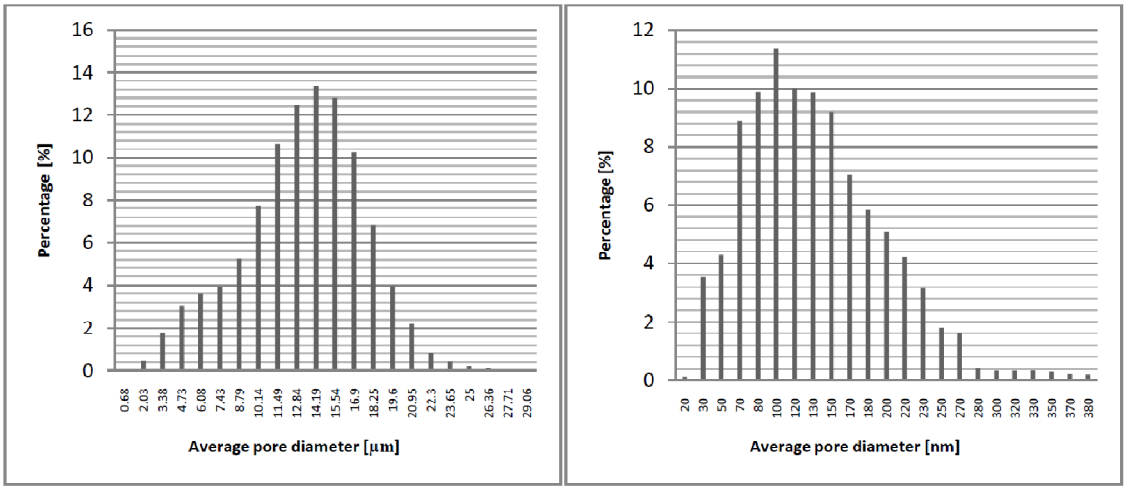

a b

Figure 5. Pore size distribution in GDL and MPL; a) Pore size distribution in GDL; b) Pore size distribution in MPL

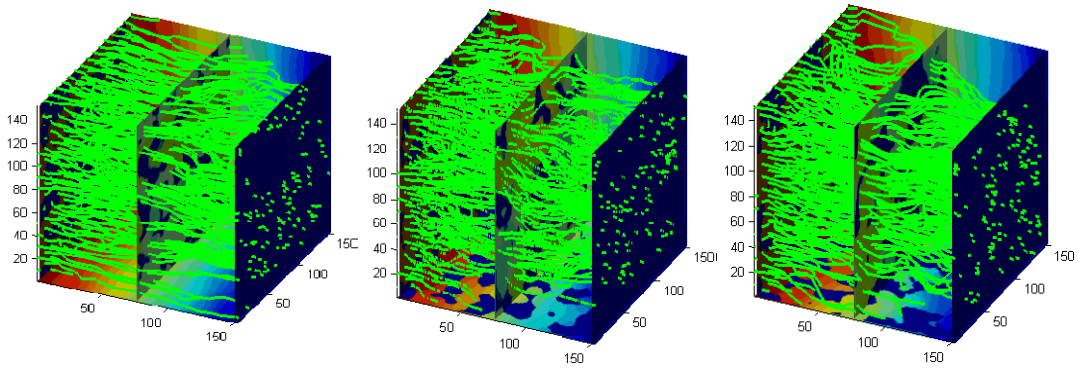

a b c

Figure 6. Tortuous flow paths simulated by the single-phase D3Q19 LB numerical solver in three planes. Units are in pixel and each pixel is 8 nm. The green lines are the paths along which the gas diffuses. The background colour is the gas concentration which decreases from red to blue. Gas flows from the left to the right in each image and a) shows the principal flow direction; b) shows the first off-principal direction; c) shows the second off-principal direction.